PAPER

In situ surface regulation of 3D perovskite using diethylammonium iodide for highly efficient perovskite solar cells†

Xiaopeng Yue,[ab] Yingying Yang,[a] Xing Zhao,[a] Bingbing Fan,[a] Huilin Yan,[a] Shujie Qu,[a] Qiang Zhang,[a] Zhineng Lan,[a] Shuxian Du,[a] Hao Huang,[a] Luyao Yan,[a] Xinxin Wang,[a] Peng Cui,[a] Junfeng Ma[a] and Meicheng Li (iD) ★[a]

Surface passivation by constructing a 2D/3D structure is considered to be an effective strategy for suppressing non-radiative recombination and improving the device efficiency and stability. Herein, the 2D perovskite is formed *in situ* on the surface of a 3D perovskite *via* chemical interactions between diethylammonium iodide (DAI) and Pb−I octahedra, which greatly reduces the deep level defects and non-radiative recombination. Moreover, the 2D/3D structure can regulate the energy level alignment, enhance the charge extraction, and improve the open-circuit voltage. Finally, compared with the control device, the power conversion efficiency (PCE) of the DAI-treated device increases from 21.58 to 23.50%. The unencapsulated devices stored in air for more than 500 hours can still retain 97% of their initial PCE, revealing good long-term placement stability. This work provides a promising strategy to fabricate efficient PSCs through the *in situ* construction of 2D/3D perovskite heterojunctions.

Introduction

Organic–inorganic metal hybrid perovskite materials are considered as promising light absorption materials due to their superb properties, which include high absorption coefficients, tunable bandgaps and long carrier lifetimes.[1–3] At present, the power conversion efficiency (PCE) of perovskite solar cells (PSCs) has been improved from 3.8 to 25.7% in only a dozen years.[4,5] Apart from their high efficiency, PSCs also have the advantages of simple fabrication and low-cost owing to their solution processibility, demonstrating their great potential for commercialization.

Perovskite films prepared using a solution method often form pinholes, cracks and a large number of defects during the crystallization process.[6] These defects include excessive uncoordinated lead halide and cation vacancies, which can lead to severe charge recombination, current hysteresis, and open circuit voltage (V_{OC}) loss in the PSCs. Especially under high humidity, high temperature and UV light, the deterioration of perovskite films and devices will be rapidly accelerated *via* trap defects.[7–9]

Therefore, a variety of strategies, such as component engineering, optimization of the preparation process and device structure, and surface engineering, have been successfully adopted and proved to be effective methods for improving the device efficiency and stability.[9–12] Passivating the perovskite surface through constructing 2D/3D mixed perovskites is considered to be an effective way of regulating the interfacial problems and suppressing the trap defects. Large amine ions, such as phenylethylamine (PEA), butylamine (BA), and quaternary amine (QA), have been applied to 3D PSCs as defect passivators that show a positive effect in reducing the trap defects.[13–17] In addition, the heterostructure of 2D/3D perovskites can regulate the band alignment which facilities charge transport at the interface.[18] Diethylamine (DA) has an amine group that can be combined with lead halide to form a 2D perovskite, while the hydrophobic aliphatic hydrocarbon chain can protect the perovskite from corrosion by water and improve the air-stability of the PSCs. Recently, some researchers have incorporated diethylammonium iodide (DAI) into perovskite precursor solutions or anti-solvents to modify the perovskite films by regulating the crystal growth process, achieving increased PCE values exceeding 20%.[19,20] However, these methods introduce new impurities that are not conducive to further improvement of the PSCs. In addition, diethylammonium bromide (DABr) has also been used in surface treatment for methylammonium lead triiodide based PSCs to fabricate high quality 2D/3D hybrid perovskite films, achieving a PCE of 18.3%.[21]

[a] *State Key Laboratory of Alternate Electrical Power System with Renewable Energy Sources, School of New Energy, North China Electric Power University, Beijing 102206, China. E-mail: mcli@ncepu.edu.cn*

[b] *School of Energy and Environmental Engineering, Hebei University of Engineering, Handan, Hebei 056038, China*

This journal is © the Owner Societies 2023

Phys. Chem. Chem. Phys., 2023, **25**, 9349–9356 | 9349

In this work, we employed DAI for the *in situ* regulation of the 3D perovskite surface. DAI was dissolved in isopropanol (IPA) and spin-coated onto a 3D perovskite. Different from doping into the precursor solution, this post-treatment method does not affect the crystallization of the bulk while it induces recrystallization near the surface. IPA can dissolve a small amount of formamidine iodide (FAI) at the as-prepared 3D perovskite ($Cs_{0.05}FA_{0.85}MA_{0.1}PbI_3$) surface, resulting in the formation of a PbI_2-rich surface, which is conducive to the reconstruction of 2D perovskite capping layer on the surface of the perovskite.[22] Compared with large aromatic cationic amine salts, small sized DAI is prone to filling the grain boundary and passivating the trap defects. This processing strategy can increase the PCE of the device from 21.58 to 23.50%, with an impressive V_{OC} of 1.154 V, a high fill factor (FF) of 81.3%, and negligible hysteresis. In particular, the DAI treated device shows good operational stability, as confirmed through the steady-state output measurement that shows little efficiency loss. In addition, after storing for 500 hours in ambient air with a relative humidity of $\sim 10\%$, unpackaged devices can still retain 97% of their initial PCE. This work provides a facile means of regulating the top surface of 3D perovskite by constructing a mixed 2D/3D perovskite heterojunction which can be applied to perovskite based photovoltaic areas.

Results and discussion

The molecular structure of DAI is shown in Fig. S1 (ESI†). With an amine group and two ethyl groups, DAI is thought to effectively passivate defects at the perovskite surface by filling the halide vacancies or binding to uncoordinated halide ions and Pb^{2+} ions. Besides, the hydrophobic aliphatic chain of DAI is expected to improve the air stability of the perovskite.

Thus, we introduce DAI on-top of the 3D perovskite layer to modify the film properties. The DAI solution was spin-coated onto the perovskite film and then annealed at 100 °C for 3 min to induce the *in situ* reconstruction of the 3D perovskite surface and the formation of the 2D perovskite (Fig. 1a).

Scanning electron microscopy (SEM) was used to explore the surface morphology change of the perovskite films before and after DAI treatment. The effects of DAI at different concentrations (0, 5, 8, 10, 15, 20 mg mL^{-1}) on the morphology of the perovskite films are shown in Fig. S2 (ESI†). A large number of PbI_2 residuals can be clearly seen on the control film (Fig. 1b and Fig. S2a, ESI†), which will act as defect centers to capture free charges, resulting in severe non-radiative recombination.[23,24] With the increase in DAI concentration, the PbI_2 phase gradually decreases until it disappears at a concentration of 10 mg mL^{-1}. With a further increase in the DAI concentration, the grains become larger, and the new phase appears clearly when the DAI concentration reaches 20 mg mL^{-1}. We prepared the n–i–p structured devices to explore the effect of DAI treatment on the photovoltaic performance of the PSCs. We firstly optimized the concentration of DAI, and the corresponding statistical photovoltaic parameters are displayed in Fig. S3 (ESI†). The photocurrent–voltage (J–V) curves of the best device for treatment with DAI at different concentrations are exhibited in Fig. S4 (ESI†). The V_{OC} shows continual improvement with the increase in DAI concentration. However, due to the excessive accumulation of 2D perovskite and the emergence of a new phase, both J_{SC} and FF decrease clearly when the DAI concentration is increased further to 15 and 20 mg mL^{-1}. As a result, we find the optimal concentration to be 10 mg mL^{-1}, and from the corresponding SEM images shown in Fig. 1c, it can be observed that the excess PbI_2 disappears and the grains become more compact. Later in this paper, unless otherwise specified, control and DAI represent the devices without and with 10 mg mL^{-1} DAI treatment, respectively.
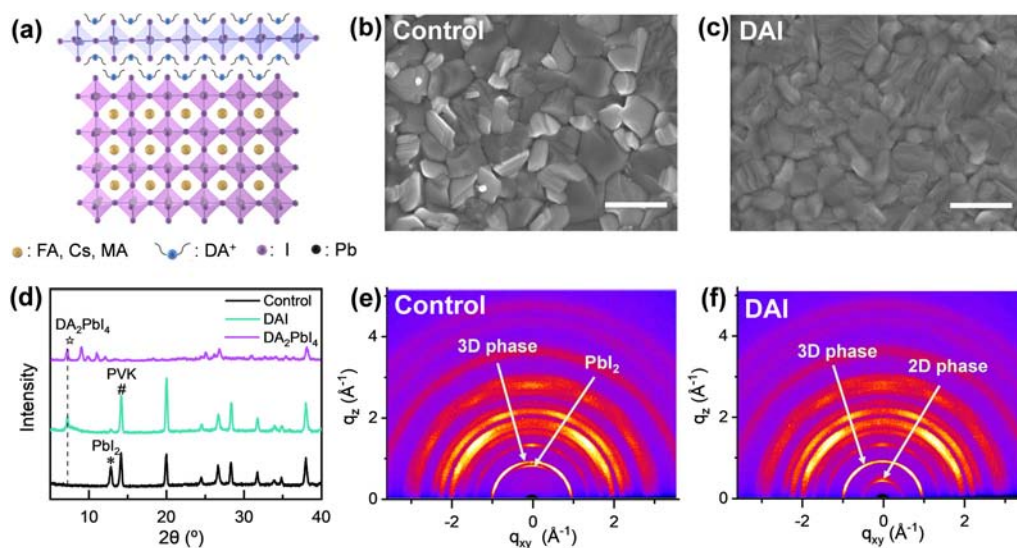

Fig. 1 (a) Schematic diagram of the DAI treated perovskite. Top-view SEM images of the (b) control and (c) DAI treated perovskite. (d) XRD patterns of the perovskite films without and with DAI treatment, and pure DA_2PbI_4. Grazing incidence X-ray diffraction (GIXRD) patterns of the (e) control and (f) DAI treated perovskite films with an incident angle of 0.5°.

9350 | *Phys. Chem. Chem. Phys.*, 2023, **25**, 9349–9356

This journal is © the Owner Societies 2023

The surface topographies of the control and DAI-treated perovskite films were further analyzed using atomic force microscopy (AFM). As shown in Fig. S5 (ESI†), the control 3D perovskite film displays a rough surface with a high root-mean-square (RMS) value of 45.06 nm. By contrast, the DAI-treated perovskite surface is more uniform and compact with a smoother (RMS = 31.05 nm) surface, which will be beneficial for charge transport between the perovskite and the hole transport layer.

To verify the 3D perovskite reconstructed *via* DAI treatment, crystal phases of the control and DAI-treated perovskite films were investigated *via* X-ray diffraction (XRD) measurements, as shown in Fig. 1d. To further validate our deduce, we also investigated pure DA_2PbI_4 (2D) perovskite film by XRD measurement as shown in Fig. 1d. For the control and DAI-treated films, the main reflections located at 14.2° correspond to the (001) crystal plane of the α-phase perovskite. After DAI treatment, a new peak at 7.2° is observed, which is in accordance with that of DA_2PbI_4, indicating the formation of the 2D perovskite layer. In addition, a strong peak at 12.8° represents the excess PbI_2 in the control perovskite film, whereas almost disappears upon DAI treatment. Grazing incidence X-ray diffraction (GIXRD) was carried out to further study the crystalline structure of the perovskites for the control and with DAI treatment. The 2D-GIXRD images of the control and the 2D/3D perovskite film are shown in Fig. 1e and f, respectively. The control film shows two obvious diffraction rings at $q = 0.993$ and 0.897 Å^{-1}, corresponding to the 3D perovskite and PbI_2, respectively. In the GIXRD pattern of the DAI-treated perovskite film, the disappearance of the PbI_2 peak accompanied by the emergence of a new diffraction ring at $q = 0.499$ Å^{-1} proves the formation of the 2D perovskite.[25] This further confirms the 2D phase formation through *in situ* surface regulation of the 3D perovskite and

excess PbI_2 removal by DAI, which is consistent with the XRD results.

The UV-vis absorption spectra of the control and DAI-treated films show that both films exhibit similar light absorption in the visible region (Fig. 2a). Fourier transform infrared (FTIR) spectroscopy and X-ray photoelectron spectroscopy (XPS) analysis were performed on the perovskite films with and without DAI treatment to investigate the interaction between DAI and the perovskite surface. The FTIR spectra acquired in attenuated total reflectance (ATR) mode are shown in Fig. 2(b and c) and the full spectra are shown in Fig. S6 (ESI†). For the control perovskite film, a strong stretching vibration of C=N from FA$^+$ appears at 1712 cm^{-1} (Fig. S6, ESI†). At the same time, peaks appearing at 3401, 3268 and 1612 cm^{-1} belong to the N–H stretching vibrations. The absorption peaks at 1352 and 1470 cm^{-1} are the umbrella and anti-symmetric bending vibrations of the methyl (CH$_3$) group, respectively.[26] After DAI treatment, new absorption peaks appear at 3024 and 766 cm^{-1}, which correspond to the symmetric stretching of the methylene (CH$_2$) group and the N–H wag from the secondary amine in DAI, respectively.[27] These new peaks indicate the successful incorporation of DAI on top of the 3D perovskite.

X-ray photoelectron spectroscopy (XPS) measurements were carried out to further explore the effect of DAI treatment on the chemical composition and structure of the perovskite film (Fig. 2d–f and Fig. S7, ESI†). As shown in Fig. 2d, C–C, C–N and C=O peaks are located at the binding energies of 284.8 eV, 286.5 eV and 288.4 eV, respectively. Due to the ethyl group and C–N–C chemical bonds in the DA$^+$ cations, the C–C and C–N peaks of the perovskite film treated with DAI are significantly enhanced. The peak at 288.4 eV (C=O) of the pristine perovskite film corresponds to the adsorption of H$_2$O and O$_2$ with exposure in air. With DAI treatment, the C=O peak of the
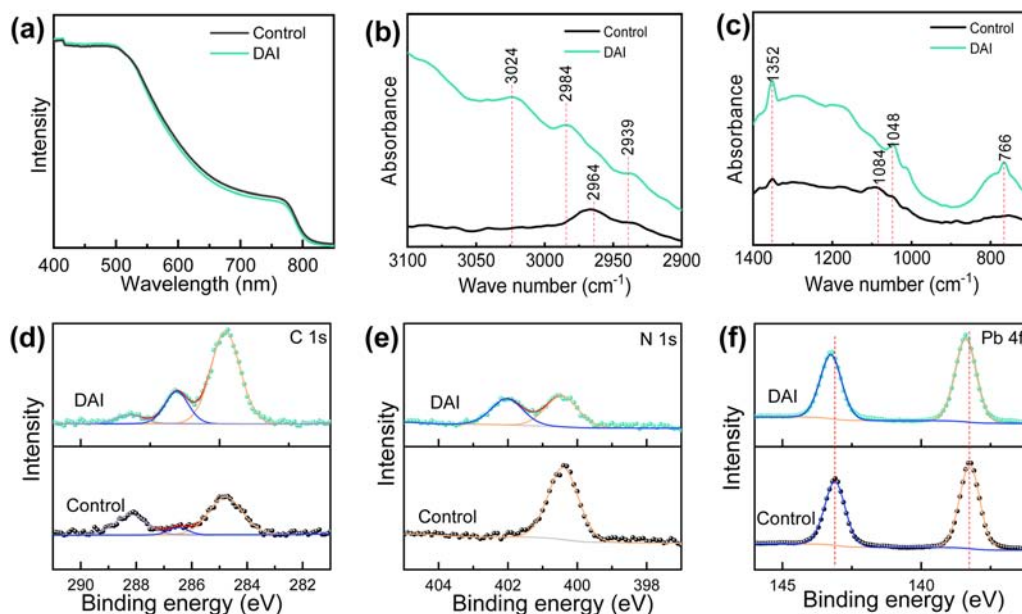

Fig. 2 (a) UV-vis absorption spectra for the control and DAI-treated perovskite films. (b and c) FTIR and (d–f) high-resolution XPS spectra of the perovskite films with and without DAI treatment.

This journal is © the Owner Societies 2023

Phys. Chem. Chem. Phys., 2023, **25**, 9349–9356 | 9351

perovskite film is suppressed, indicating the inhibition of H_2O and O_2 adsorption, which is more conducive to improving the water stability of the perovskite film. We further observe a single peak at 400.3 eV in the N 1s spectrum for the 3D pristine film, whereas two peaks, located at 400.3 eV and 402.0 eV, for the DAI-treated film are observed (Fig. 2e). The C═N peak at 400.3 eV is derived from FA^+, while the other C–N peak at 402.0 eV is derived from DA^+. Besides that, the peak position of Pb $4f_{7/2}$ and Pb $4f_{5/2}$ is shifted 0.15 eV towards a higher binding energy after DAI treatment, as shown in Fig. 2f, implying the chemical interaction between DAI and the perovskite. The I 3d signals remain unchanged, as shown in Fig. S7b (ESI†).

Fig. 3a displays the energy level diagrams of the control and DAI-treated perovskite films, as determined using ultraviolet photoelectron spectroscopy (UPS) (Fig. 3b). The 3D control perovskite exhibits a Fermi level (E_F) of −5.04 eV and a valence band (VB) of −6.11 eV. Meanwhile, the E_F and VB values are −4.99 and −6.00 eV, respectively, for the DAI treated perovskite film. The slightly upshifted VB of the 2D/3D perovskite will alleviate the energy level mismatch with the highest occupied molecular orbital (HOMO) level of the hole transport layer (HTL). The improved band alignment between the perovskite and the HTL facilitates the hole extraction and energy loss reduction, which is associated with the enhanced V_{OC} of PSCs, thus improving the overall device performances.[28,29] Furthermore, Kelvin probe force microscopy (KPFM) measures the contact potential difference between the surface of a solid-state sample and the probe, as shown in Fig. 3c and d. The RMS value of the surface potential decreases from 19.98 to 4.04 mV. A homogeneous and uniform distribution of the surface potential is beneficial for effective charge carrier extraction to prevent non-radiative recombination, which means that the defects enriched at the 3D perovskite grain boundaries are significantly eliminated.[30,31]

As can be seen in Fig. 4a, the cross-sectional SEM image of the DAI-treated perovskite film shows that it is hole-free and dense compared with the reference sample. The steady-state photoluminescence (SSPL) intensity of the glass/perovskite/DAI film is higher than that of the glass/perovskite film (Fig. 4b), indicating that DAI can effectively reduce the non-radiative recombination loss. According to the previous statement, this enhancement can be attributed to the depletion of excess PbI_2 as well as DAI induced trap passivation. We further collected the time-resolved photoluminescence (TRPL) spectra to investigate the effect of DAI on the carrier characteristics of the perovskite film (Fig. 4c). The TRPL spectrum was fitted according to the following equation:[8]

$$I(t) = I_0 + A_1 \exp(-t/(\tau_1)) + A_2 \exp(-t/\tau_2) \qquad (1)$$

where A_1 and A_2 represent the amplitude of the fast and slow decay processes, respectively, and τ_1 and τ_2 are the fast and slow decay time constants, respectively. The average carrier lifetime are calculated according to the following equation:[32]

$$\tau_{ave} = (A_1\tau_1{}^2 + A_2\tau_2{}^2)/(A_1\tau_1 + A_2\tau_2). \qquad (2)$$

All the fitted time decay parameters are summarized in Table S1 (ESI†). The DAI-treated perovskite film exhibits a slower PL decay with a τ_1 of 0.27 μs and a τ_2 of 1.77 μs, whereas the control perovskite film presents a τ_1 of 0.23 μs and a τ_2 of 1.64 μs. The average carrier lifetime increases from 1.60 μs to 1.75 μs. The longer lifetime of the DAI-treated perovskite film suggests the suppressed non-radiative recombination.

Moreover, electrical impedance spectroscopy (EIS) measurements were conducted to investigate the electrical characteristics of the device. Nyquist plots of the control and DAI-treated devices were measured at an applied voltage of 1.0 V under dark
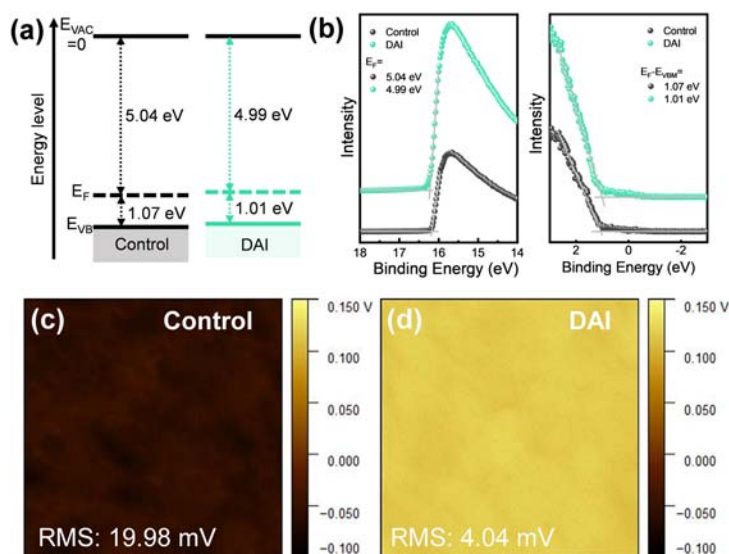

Fig. 3 (a) Schematic energy level diagrams for the control and DAI-treated perovskite films. (b) UPS profiles of the control and DAI-treated films. (c and d) KPFM surface potential maps of the control and DAI-treated films.

9352 | *Phys. Chem. Chem. Phys.*, 2023, **25**, 9349–9356

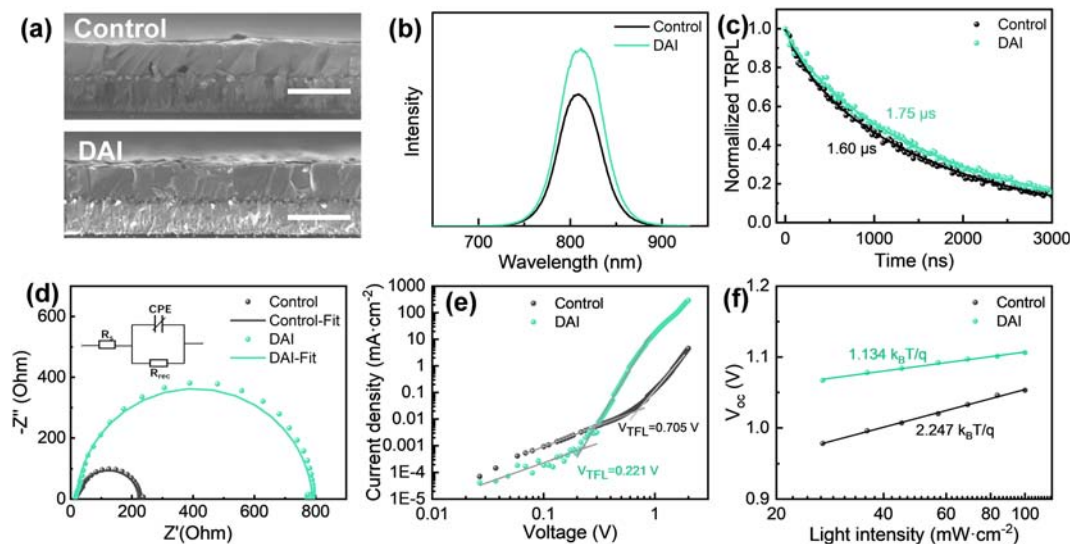This journal is © the Owner Societies 2023

Fig. 4 (a) Cross-sectional SEM images of the control device and the DAI-treated device. (b) SSPL and (c) TRPL spectra of the control and DAI-treated perovskite films on glass substrates. (d) Nyquist plots of the electrical impedance spectroscopy (EIS) of the control device and the DAI-treated device with a −1 V bias voltage under dark conditions. (e) Dark J−V curves of the electron-only devices with the structures of FTO/TiO$_2$/perovskite/PCBM/Au and FTO/TiO$_2$/perovskite/DAI/PCBM/Au. (f) Light-dependent V_{OC} changes of the control device and the DAI-treated device.

conditions (Fig. 4d). The EIS data are fitted according to the equivalent circuit (inset of Fig. 4d), in which CPE is the constant phase element representing the capacitance, R_s represents the series resistance, and R_{rec} represents the recombination resistance of the device – the corresponding results are listed in Table S2 (ESI†). Compared with the control device, the DAI device has a lower R_s of 18.22 Ω and a larger R_{rec} of 772 Ω. The decrease in the series resistance may be attributed to the better contact between the perovskite film and the hole transport layer, resulting in a higher V_{OC}. The increase in recombination resistance may be attributed to passivation of the perovskite surface defects and an enhancement of the charge extraction ability,[33] which results in a higher V_{OC}. Both changes in R_s and the R_{rec} are beneficial for charge transfer, resulting in a larger FF and a better PCE. The defect density of the perovskite films is quantitatively calculated through the dark J–V curves of the electron-only devices (Fig. 4e). The defect density is calculated according to the following equation:[34]

$$n_{traps} = 2V_{TFL}\varepsilon\varepsilon_0/el^2 \tag{3}$$

where n_{traps} is the density of trap states, V_{TFL} is the trap-filled limit voltage, ε is the dielectric constant of the perovskite, ε_0 is the permittivity of a vacuum, e is the elementary charge and l is the thickness of the perovskite film. According to the fitted dark J–V curves, the V_{TFL} of the control and DAI-treated perovskite films are 0.705 and 0.221 V, respectively.[35] The defect density of the DAI-treated perovskite film is calculated to be 2.14 × 10^{15} cm^{-3}, which is much lower than that of the control film (7.84 × 10^{15} cm^{-3}), indicating the efficient defect passivation of the DAI induced 2D perovskite capping layer. The dependence of V_{OC} on the light intensity is analyzed to obtain further insight into the trap-assisted charge recombination of the devices.[36] As shown in Fig. 4f, under the same light intensity,

the V_{OC} of the DAI-treated device is higher than that of the control device, and both devices show a linear relationship between V_{OC} and the light intensity. The slope of the control and DAI-treated devices is 2.247 k_BT/q and 1.134 k_BT/q, respectively, in which k_B is the Boltzmann constant, T is the temperature and q is the electric charge. The lower slope confirms that the trap-assisted charge recombination of the DAI modified device is much smaller than that of the control device.[37] Improved carrier transport and reduced carrier non-radiative recombination are responsible for the improved performance of the PSCs with DAI treatment.

Finally, the statistical photovoltaic performances of 30 PSCs including PCE, V_{OC}, J_{SC} and FF for both the reverse and forward scan directions are shown in Fig. 5a–d. The corresponding statistics and champion parameters are summarized in Table 1. The apparent increase in V_{OC} can be attributed to the energy band alignment, the decrease in non-radiative recombination and the increase of the carrier lifetime, which are derived from the DAI induced *in situ* regulation of the perovskite surface and defect passivation. Besides, the hysteresis index (HI) is defined using the following equation:

$$HI = (PCE_{reverse} - PCE_{forward})/PCE_{reverse}. \tag{4}$$

The HI of the DAI-treated PSCs was significantly reduced compared with that of the control PSCs, and the average hysteresis index (HI) of the control and DAI-treated devices was 0.17 and 0.05, respectively (Fig. 5e). The possible reason is that ion migration in the device is reduced through effective passivation of the 2D layer as well as effective elimination of excess PbI$_2$. This is highly consistent with previous research in which the 2D perovskite capping layer formed atop a 3D perovskite film can effectively block ion migration and reduce the hysteresis of the PSCs.[38,39]

The typical J–V curves of the best performing PSCs for the control and DAI-treated PSCs measured under different scan
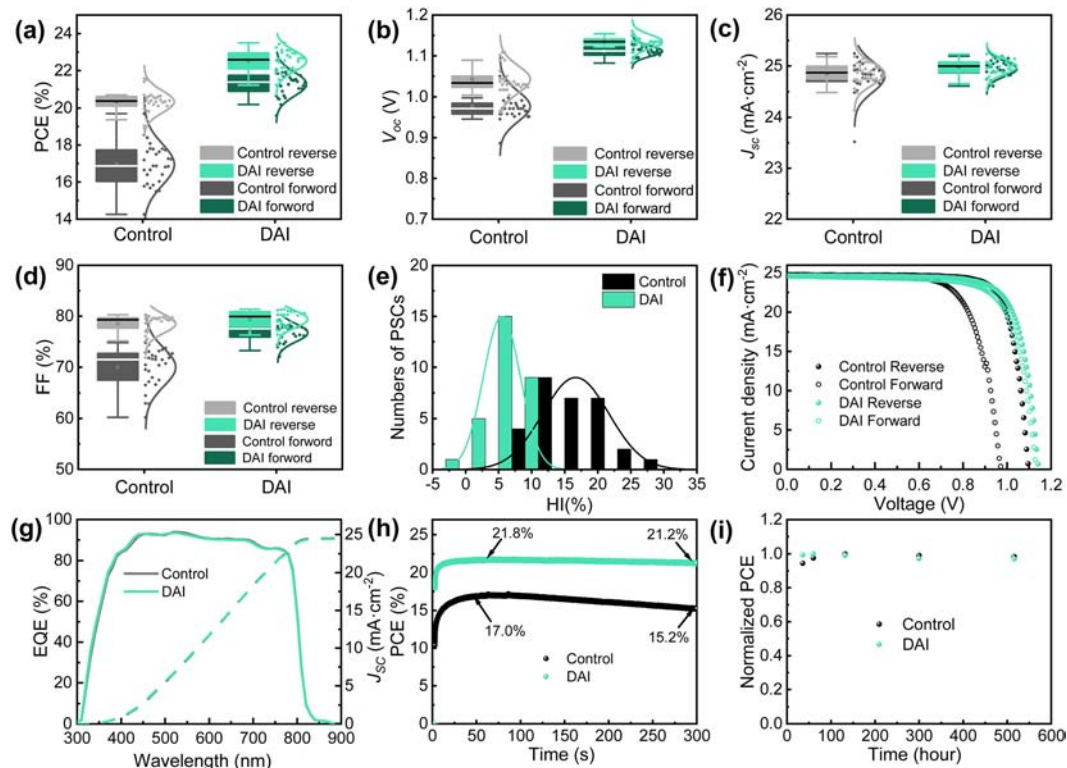
Fig. 5 Reverse and forward scan statistical distributions of the (a) PCE, (b) V_{OC}, (c) J_{SC}, and (d) FF values, and (e) the HI, for 30 devices with and without DAI treatment. (f) Typical $J-V$ curves for best performing devices with and without DAI treatment. (g) Corresponding EQE curves. (h) Stabilized PCE measured at the maximum power point. (i) Air stability of the PSCs at a humidity of ∼10%.

Table 1 $J-V$ parameters of the PSCs with and without DAI-treatment. These data are extracted from 30 devices

Sample	Scan direction		V_{OC} (V)	J_{SC} (mA cm^{-2})	FF (%)	PCE (%)
Control	Reverse	Average Champion	1.043 ± 0.033 (1.096)	24.85 ± 0.22 (24.73)	78.5 ± 1.9 (79.6)	20.34 ± 0.60 (21.58)
	Forward	Average Champion	0.977 ± 0.037 (0.971)	24.79 ± 0.30 (24.67)	70.0 ± 3.7 (78.8)	16.94 ± 1.12 (17.19)
DAI	Reverse	Average Champion	1.135 ± 0.017 (1.154)	24.98 ± 0.14 (25.04)	79.4 ± 1.6 (81.3)	22.52 ± 0.56 (23.50)
	Forward	Average Champion	1.111 ± 0.013 (1.115)	24.94 ± 0.15 (25.05)	76.7 ± 1.8 (78.0)	21.28 ± 0.63 (21.80)

directions are shown in Fig. 5f. The PCE of the optimal control device is 21.58%, with a V_{OC} of 1.096 V, a J_{SC} of 24.73 mA cm^{-2} and an FF of 79.6%. By contrast, the optimal DAI-treated PSC shows a V_{OC} of 1.154 V, a J_{SC} of 25.04 mA cm^{-2} and an FF of 81.3%, resulting in a champion PCE of 23.50%, which is much higher than that of the control device.

The external quantum efficiency (EQE) curves of the control and DAI-treated devices are shown in Fig. 5g. The integrated J_{SC} values of the control and DAI-treated PSCs are 24.46 and 24.43 mA cm^{-2}, respectively, which match well with the values measured from the $J-V$ curves. To further investigate the photovoltaic performance of the devices, the time-dependent stabilized PCE of the PSCs with the control and DAI-treated perovskite layers was measured at the maximum power point (MPP), as shown in Fig. 5h. For the DAI-treated device, the stabilized PCE decreases by only 2.75% during the first 300 s while that of the control device decreases by 10.59%. In addition, after storing for 500 hours in ambient air with a relative humidity of ∼10%, both unpackaged devices can still retain 97% of their initial PCE (Fig. 5i), delivering good long-term ambient stability.

Conclusions

In summary, we successfully employed DAI as organic spacer group to construct mixed 2D/3D perovskites for efficient PSCs. The deposition of DAI can induce the *in situ* regulation of a 3D perovskite through the chemical reaction of DAI and excess PbI$_2$. Upon incorporation of the DAI, the excess PbI$_2$ in the perovskite film is consumed by forming a 2D perovskite, which greatly reduces the defect density and non-radiative recombination of the perovskite film. Moreover, the 3D/2D structure can regulate the energy level alignment, enhance the charge extraction, and improve the V_{OC}. As a result, a PCE of 23.50% for the DAI-treated device is achieved with small hysteresis,

9354 | *Phys. Chem. Chem. Phys.*, 2023, **25**, 9349–9356

This journal is © the Owner Societies 2023

compared with the control device with an efficiency of 21.58%. In addition, after storing for 500 hours in ambient air with a relative humidity of ~10%, the unpackaged devices still retain >97% of their initial PCE. The dramatic improvement of the photovoltaic performance confirms that the appropriate reconstruction of 2D/3D perovskites using DAI is an important strategy for the development of PSCs with high efficiency and stability.

Author contributions

X. Y. and Y. Y. contributed equally to this work. X. Y. was responsible for the experiments and data collection. Y. Y. finished the data analysis and wrote the paper. S. Q. Q. Z., Z. L., S. D., H. H., L. Y., H. Y. and X. W. were involved in the sample preparation. X. Z., B. F., P. C. and J. M. were involved in discussions on the data analysis and interpretation. M. L. directed and supervised the project.

Conflicts of interest

There are no conflicts to declare.

Acknowledgements

References

1 S. De Wolf, J. Holovsky, S. J. Moon, P. Loper, B. Niesen, M. Ledinsky, F. J. Haug, J. H. Yum and C. Ballif, *J. Phys. Chem. Lett.*, 2014, **5**, 1035–1039.

2 J. Xue, Z. Wang, A. Comstock, Z. Wang, H. H. Y. Sung, I. D. Williams, D. Sun, J. Liu and H. Lu, *Chem. Mater.*, 2022, **34**, 2813–2823.

3 N. G. Park, *Adv. Energy Mater.*, 2019, **10**, 1903106.

4 A. Kojima, K. Teshima, Y. Shirai and T. Miyasaka, *J. Am. Chem. Soc.*, 2009, **131**, 6050–6051.

5 NREL, Best Research Cell Efficiency Chart.

6 B. Chen, P. N. Rudd, S. Yang, Y. Yuan and J. Huang, *Chem. Soc. Rev.*, 2009, **48**, 3842–3867.

7 C. X. Ran, J. T. Xu, W. Y. Gao, C. M. Huang and S. X. Dou, *Chem. Soc. Rev.*, 2018, **47**, 4581–4610.

8 J. Chen, X. Zhao, S. G. Kim and N. G. Park, *Adv. Mater.*, 2019, **39**, 1902902.

9 Q. Jiang, Y. Zhao, X. W. Zhang, X. L. Yang, Y. Chen, Z. M. Chu, Q. F. Ye, X. X. Li, Z. G. Yin and J. B. You, *Nat. Photonics*, 2019, **13**, 460–466.

10 M. Kim, G. H. Kim, T. K. Lee, I. W. Choi, H. W. Choi, Y. Jo, Y. J. Yoon, J. W. Kim, J. Lee, D. Huh, H. Lee, S. K. Kwak, J. Y. Kim and D. S. Kim, *Joule*, 2019, **3**, 2179–2192.

11 H. Huang, P. Cui, Y. Chen, L. Yan, X. Yue, S. Qu, X. Wang, S. Du, B. Liu, Q. Zhang, Z. Lan, Y. Yang, J. Ji, X. Zhao, Y. Li, X. Wang, X. Ding and M. Li, *Joule*, 2022, **6**, 1–17.

12 P. Cui, D. Wei, J. Ji, H. Huang, E. D. Jia, S. Y. Dou, T. Y. Wang, W. J. Wang and M. C. Li, *Nat. Energy*, 2019, **4**, 150–159.

13 N. Li, Z. L. Zhu, Q. S. Dong, J. W. Li, Z. L. Yang, C. C. Chueh, A. K. Y. Jen and L. D. Wang, *Adv. Mater. Interfaces*, 2017, **4**, 1700598.

14 Y. H. Hu, J. Schlipf, M. Wussler, M. L. Petrus, W. Jaegermann, T. Bein, P. Muller-Buschbaum and P. Docampo, *ACS Nano*, 2016, **10**, 5999–6007.

15 H. S. Yoo and N. G. Park, *Sol. Cells*, 2018, **179**, 57–65.

16 X. P. Zheng, B. Chen, J. Dai, Y. J. Fang, Y. Bai, Y. Z. Lin, H. T. Wei, X. C. Zeng and J. S. Huang, *Nat. Energy*, 2017, **2**, 17102.

17 F. Wang, W. Geng, Y. Zhou, H. H. Fang, C. J. Tong, M. A. Loi, L. M. Liu and N. Zhao, *Adv. Mater.*, 2016, **28**, 9986–9992.

18 Y. Lin, Y. Bai, Y. J. Fang, Z. L. Chen, S. Yang, X. P. Zheng, S. Tang, Y. Liu, J. J. Zhao and J. S. Huang, *J. Phys. Chem. Lett.*, 2018, **9**, 654–658.

19 X. Huang, Q. Cui, W. Bi, L. Li, P. Jia, Y. Hou, Y. Hu, Z. Lou and F. Teng, *RSC Adv.*, 2019, **9**, 7984–7991.

20 X. Huang, W. Bi, P. Jia, Q. Cui, Y. Hu, Z. Lou, Y. Hou and F. Teng, *ACS Appl. Mater. Interfaces*, 2020, **12**, 16707–16714.

21 X. Huang, W. Bi, P. Jia, Y. Tang, Z. Lou, Y. Hu, Q. Cui, Y. Hou and F. Teng, *Org. Electron.*, 2019, **67**, 101–108.

22 C. Y. Deng, J. H. Wu, Y. T. Du, Q. Chen, Z. Y. Song, G. D. Li, X. B. Wang, J. M. Lin, W. H. Sun, M. L. Huang, Y. F. Huang, P. Gao and Z. Lan, *Small Methods*, 2021, **5**, 2101000.

23 Y. Rao, Z. Li, D. Liu, C. Chen, X. Wang, G. Cui and S. Pang, *ACS Appl. Mater. Interfaces*, 2021, **13**, 20043–20050.

24 J. Schoonman, *Chem. Phys. Lett.*, 2015, **619**, 193–195.

25 H. Kim, S. U. Lee, D. Y. Lee, M. J. Paik, H. Na, J. Lee and S. I. Seok, *Adv. Energy Mater.*, 2019, **9**, 1902740.

26 P. L. Qin, G. Yang, Z. W. Ren, S. H. Cheung, S. K. So, L. Chen, J. Hao, J. Hou and G. Li, *Adv. Mater.*, 2018, **30**, 1706126.

27 S. Palei, H. Kim, J. H. Seo, D. Singh and K. Seo, *Adv. Mater. Interfaces*, 2022, **9**, 2200464.

28 H. Zhou, Q. Chen, G. Li, S. Luo, T. B. Song, H. S. Duan, Z. Hong, J. You, Y. Liu and Y. Yang, *Science*, 2014, **345**, 542–546.

29 P.-C. Huang, S.-K. Huang, T.-C. Lai, M.-C. Shih, H.-C. Hsu, C.-H. Chen, C.-C. Lin, C.-H. Chiang, C.-Y. Lin and K. Tsukagoshi, *Nano Energy*, 2021, **89**, 106362.

30 J. Ciro, S. Mesa, J. I. Uribe, M. A. Mejia-Escobar, D. Ramirez, J. F. Montoya, R. Betancur, H. S. Yoo, N. G. Park and F. Jaramillo, *Nanoscale*, 2017, **9**, 9440–9446.

This journal is © the Owner Societies 2023

Phys. Chem. Chem. Phys., 2023, **25**, 9349–9356 | **9355**

31 J. J. Yoo, S. Wieghold, M. C. Sponseller, M. R. Chua, S. N. Bertram, N. T. P. Hartono, J. S. Tresback, E. C. Hansen, J.-P. Correa-Baena, V. Bulović, T. Buonassisi, S. S. Shin and M. G. Bawendi, *Energy Environ.*, 2019, **12**, 2192–2199.

32 D.-Y. Son, J.-W. Lee, Y. J. Choi, I.-H. Jang, S. Lee, P. J. Yoo, H. Shin, N. Ahn, M. Choi, D. Kim and N.-G. Park, *Nat. Energy*, 2016, **1**, 10681.

33 H. Bi, X. Zuo, B. Liu, D. He, L. Bai, W. Wang, X. Li, Z. Xiao, K. Sun, Q. Song, Z. Zang and J. Chen, *J. Mater. Chem. A*, 2021, **9**, 3940–3951.

34 A. A. Zhumekenov, M. I. Saidaminov, M. A. Haque, E. Alarousu, S. P. Sarmah, B. Murali, I. Dursun, X. H. Miao, A. L. Abdelhady, T. Wu, O. F. Mohammed and O. M. Bakr, *ACS Energy Lett.*, 2016, **1**, 32–37.

35 D. Y. Son, S. G. Kim, J. Y. Seo, S. H. Lee, H. Shin, D. Lee and N. G. Park, *J. Am. Chem. Soc.*, 2018, **140**, 1358–1364.

36 S. R. Cowan, A. Roy and A. J. Heeger, *Phys. Rev. B: Condens. Matter Mater. Phys.*, 2010, **82**, 245207.

37 G. J. A. H. Wetzelaer, M. Scheepers, A. M. Sempere, C. Momblona, J. Avila and H. J. Bolink, *Adv. Mater.*, 2015, **27**, 1837–1841.

38 M. He, J. Liang, Z. Zhang, Y. Qiu, Z. Deng, H. Xu, J. Wang, Y. Yang, Z. Chen and C.-C. Chen, *J. Mater. Chem. A*, 2020, **8**, 25831–25841.

39 X. Q. Jiang, J. F. Zhang, S. Ahmad, D. D. Tu, X. Liu, G. Q. Jia, X. Guo and C. Li, *Nano Energy*, 2020, **75**, 104892.

9356 | *Phys. Chem. Chem. Phys.*, 2023, **25**, 9349–9356

This journal is © the Owner Societies 2023